INTERNATIONAL JOURNAL FOR NUMERICAL METHODS IN FLUIDS, VOL. 12, 59–80 (1991)

THERMOCAPILLARY FLOW AND NATURAL CONVECTION IN A MELT COLUMN WITH AN UNKNOWN MELT/SOLID INTERFACE

C. W. LAN AND SINDO KOU

Department of Materials Science and Engineering, and Center of Excellence in Solidification Processing Technologies of Engineering Materials, University of Wisconsin, Madison, WI 53706, U.S.A.

SUMMARY

A vertical melt column set up between an upper heating rod and a lower sample rod, i.e. the so-called half-zone system, is a convenient experimental tool for studying convection in the melt in floating-zone crystal growth. In order to help understand the convection observed in the melt column, a computer model has been developed to describe steady state, axisymmetrical thermocapillary flow and natural convection in the melt. The governing equations and boundary conditions are expressed in general non-orthogonal curvilinear co-ordinates in order to accurately treat the unknown melt/solid interface as well as all other physical boundaries in the system. The effects of key dimensionless variables on the following items are discussed: (1) convection and temperature distribution in the melt; (2) the shape of the melt/solid interface; (3) the height of the melt column. These dimensionless variables are the Grashof, Marangoni and Prandtl numbers.

KEY WORDS Thermocapillary flow Natural convection Melt/solid interface Grashof number Marangoni number Prandtl number

INTRODUCTION

In a recent study by Lan *et al.*,[1] thermocapillary flow in floating-zone crystal growth under microgravity was studied in a vertical melt column of $NaNO_3$. The top of a vertical $NaNO_3$ sample rod was brought into contact with the bottom of a vertical heating rod of the same diameter and a melt column was produced at the top of the sample rod. The study focused on the reduction in thermocapillary flow in the melt column by using a ring whose inner surface was in contact with the melt surface from the top to a short distance above the melt/solid interface.

The experimental arrangement described above, i.e. to prepare a vertical melt column between a heating rod and a solid sample rod, is called a half-zone system. It was first used in a study by Schwabe *et al.*[2] There is another version of the half-zone system in which a column of melt (or organic fluid) is maintained between the ends of two vertical heating rods of the same diameter.[3–12] Under this circumstance no melting of solid sample rods is involved and hence no melt/solid interfaces are present. The main advantage of the half-zone system is that a transparent melt material (or fluid) can be used so that convection in the melt (or fluid) can be visualized. This is because, unlike in actual floating-zone crystal growth, the heater in the half-zone system is above rather than around the melt (or fluid). Of the two versions of the half-zone system mentioned above, we prefer the first one since a free boundary, i.e. the interface between the melt and the sample rod, exists in the system, thus simulating the melt/crystal interface in floating-zone crystal growth.

0271–2091/91/010059–22$11.00

Received 18 May 1989
Revised 21 November 1989

Numerous computational studies have been carried out to investigate thermocapillary flow in a melt (or fluid) column between two heating or sample rods.[13-27] Heat transfer, fluid flow and in some cases mass transfer and the effect of rotation are considered, the Prandtl numbers being mostly small, e.g. 0·1. In these studies both of the two melt/rod interfaces are assumed flat and their positions are fixed. In other words, they are mathematically identical (in the case of two heating rods) or equivalent (in the case of two sample rods) to the second version of the half-zone system mentioned above. However, there have been no computational studies on the first version of the half-zone system mentioned above. The purpose of the present study is to develop a computer model for the first version of the half-zone system, which we wish would be useful for interpreting the melt convection observed in this version of the system. The problem in the present study is computationally different from those involving the Bridgman process mainly in that Marangoni convection is not present in the Bridgman process.

In the study of Lan *et al.*[1] the effect of the contact between the melt and the inner surface of a ring on thermocapillary flow in the melt was demonstrated experimentally and with the help of some computational results. No details of the computation, however, were given. In the present study both thermocapillary flow and natural convection in a half-zone system are considered. The co-ordinate transformation, the method of solution and the treatment of the unknown melt/solid interface are described. The effects of key dimensionless variables such as the Grashof, Marangoni and Prandtl numbers are discussed.

GOVERNING EQUATIONS AND BOUNDARY CONDITIONS

The half-zone system modelled is illustrated schematically in Figure 1. The convection in the melt is assumed axisymmetric, laminar and at steady state. In the absence of flow instability caused by very strong thermocapillary flow in the melt, this assumption is considered valid. The free surface of the melt column is assumed cylindrical. Since the melt columns in most half-zone experiments are rather short, melt surface distortions are small. For example, Figure 2 shows a melt column between a 6 mm diameter $NaNO_3$ sample rod and a graphite heating rod of the same diameter. The static Bond number, which can be defined as $\rho g R^2/\gamma$ and which is often used as a measure for the extent of surface distortion due to gravity, has a relatively small value of 1·4 in this case. Melt surface distortions will be considered elsewhere.

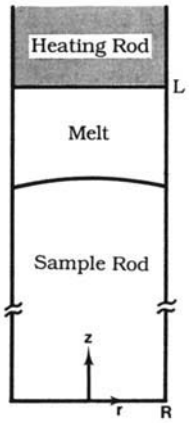

Figure 1. The half-zone system with an unknown melt/solid interface

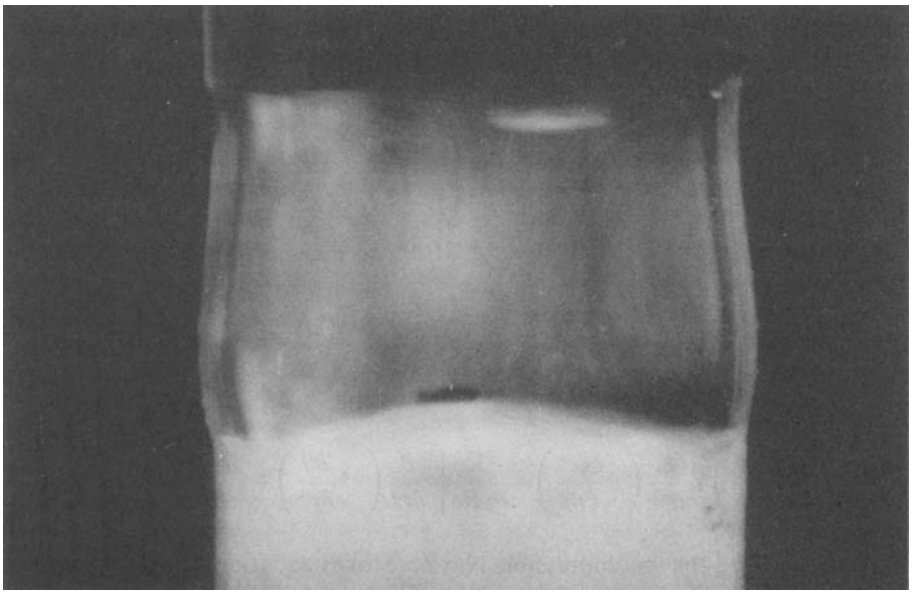

Figure 2. Melt column between an $NaNO_3$ sample rod and a graphite heating rod, both rods being 6 mm in diameter

The half-zone system being considered is illustrated schematically in Figure 1. In order to present the calculated results in dimensionless form, the following dimensionless variables are defined:

$$Re = UR/\nu, \qquad Pr = \nu/\alpha, \qquad Ma = (\partial\gamma/\partial T)\Delta T R/\rho_L \nu^2,$$
$$Gr = g\beta\Delta T R^3/\nu^2, \qquad Bi = hR/k, \qquad \theta = (T - T_m)/\Delta T,$$
$$k^* = k/k_L, \qquad \rho^* = \rho/\rho_L,$$
$$z^* = z/R, \qquad r^* = r/R, \qquad L^* = L/R,$$
$$\psi^* = \psi/\rho_L U R^2, \qquad \omega^* = \omega R/U,$$
$$u^* = u/U, \qquad v^* = v/U.$$

The above definition of the Marangoni number Ma has been used, for instance, by Derby[28] and Brown.[29] The characteristic velocity U and the characteristic temperature difference ΔT are defined as

$$U = \left(\frac{(\partial\gamma/\partial T)^2 (\Delta T)^2}{\rho_L^2 \nu R} \right)^{1/3}, \qquad \Delta T = T_h - T_m.$$

The above definition of the characteristic velocity U was first used by Ostrach[30] and more recently by Kozhoukharova *et al.*[31] The streamfunction ψ and vorticity ω are defined in terms of the radial velocity u and the axial velocity v as follows:

$$u = -\frac{1}{\rho_L r}\frac{\partial\psi}{\partial z}, \qquad v = \frac{1}{\rho_L r}\frac{\partial\psi}{\partial r}, \tag{1}$$

$$\omega = \frac{\partial u}{\partial z} - \frac{\partial v}{\partial r}. \tag{2}$$

Using the above dimensionless variables, the governing equations[32] can be expressed as follows:

equation of motion

$$\frac{\partial}{\partial r^*}\left(\frac{\omega^*}{r^*}\frac{\partial \psi^*}{\partial z^*}\right)-\frac{\partial}{\partial z^*}\left(\frac{\omega^*}{r^*}\frac{\partial \psi^*}{\partial r^*}\right)+\frac{1}{Re}\left[\frac{\partial}{\partial r^*}\left(\frac{1}{r^*}\frac{\partial(r^*\omega^*)}{\partial r^*}\right)+\frac{\partial}{\partial z^*}\left(\frac{1}{r^*}\frac{\partial(r^*\omega^*)}{\partial z^*}\right)\right]-\frac{Gr}{Re^2}\frac{\partial \theta}{\partial r^*}=0; \tag{3}$$

stream equation

$$\frac{\partial}{\partial r^*}\left(\frac{1}{\rho^* r^*}\frac{\partial \psi^*}{\partial r^*}\right)+\frac{\partial}{\partial z^*}\left(\frac{1}{\rho^* r^*}\frac{\partial \psi^*}{\partial z^*}\right)+\omega^*=0; \tag{4}$$

equation of energy

$$\frac{\partial}{\partial r^*}\left(\theta\frac{\partial \psi^*}{\partial z^*}\right)-\frac{\partial}{\partial z^*}\left(\theta\frac{\partial \psi^*}{\partial r^*}\right)+\frac{1}{PrRe}\left[\frac{\partial}{\partial r^*}\left(r^*\frac{\partial \theta}{\partial r^*}\right)+\frac{\partial}{\partial z^*}\left(r^*\frac{\partial \theta}{\partial z^*}\right)\right]=0. \tag{5}$$

Equation (3) is based on the incompressible Navier–Stokes equations employing the Boussinesq assumption.

The thermal boundary conditions are as follows.

1. Along the centreline of the system,

$$\frac{\partial \theta}{\partial r^*}=0 \quad \text{due to symmetry.}$$

2. On the surfaces of the sample rod and the free surface of the melt,

$$-(\mathbf{n}\cdot\nabla^*\theta)=Bi(\theta-\theta_a),$$

where $\mathbf{n}$ is the outward normal unit vector. A radiation term can be included on the RHS of the above equation. For a low-temperature material such as $NaNO_3$ (melting point $T_m=306{\cdot}8°C$), however, this is not necessary.

3. At the melt/heater interface,

$$\theta=1.$$

4. At the melt/solid interface,

$$\theta=0, \qquad (k^*\mathbf{n}\cdot\nabla^*\theta)_S-(\mathbf{n}\cdot\nabla^*\theta)_L+\frac{\rho_S\Delta H}{k_L\Delta T}\mathbf{n}\cdot\mathbf{V}=0.$$

The above energy balance equation is the Stefan condition. Since the sample rod does not move, velocity $\mathbf{V}=0$.

The fluid fow boundary conditions are as follows.

1. Along the melt centreline,

$$\psi^*=0, \qquad \omega^*=0.$$

2. On the melt free surface,

$$\psi^*=0, \qquad \omega^*=-(Ma)^{1/3}\frac{\partial \theta}{\partial z^*}.$$

3. At the melt/heater interface,

$$\psi^* = 0, \qquad \omega^* = \frac{\partial}{\partial z^*}\left(-\frac{1}{r^*}\frac{\partial \psi^*}{\partial z^*}\right).$$

4. At the melt/solid interface,

$$\psi^* = 0, \qquad \omega^* = \frac{\partial u^*}{\partial z^*} - \frac{\partial v^*}{\partial r^*} \quad \text{with } u^* = v^* = 0.$$

Along the melt centreline, ψ^* is set equal to zero as a reference. Along other boundaries, $\psi^* = 0$ because the sample rod is stationary. $\omega^* = 0$ in boundary condition 1 is a result of the fact that the velocity field is symmetrical with respect to the centreline (i.e. $\partial v/\partial r = 0$) and that no material flows across the centreline (i.e. $u = 0$). In boundary condition 2, $u = 0$ at the melt surface and the shear stress induced by the surface tension gradient at the melt surface is described by

$$\mu\omega = -\mu\frac{\partial v}{\partial r} = -\frac{\partial \gamma}{\partial T}\frac{\partial T}{\partial z}.$$

The vorticity boundary condition in 3 is the result of the no-slip condition $v = 0$. The no-slip condition of $u = v = 0$ is also used in boundary condition 4.

CO-ORDINATE TRANSFORMATION

Owing to the fact that the melt/solid interface is not flat but is curved, its vorticity boundary condition in terms of the cylindrical co-ordinate system (r^*, z^*), i.e. fluid flow boundary condition 4, cannot be properly implemented. In view of this, we have transformed the above governing equations and boundary conditions into those in terms of general (non-orthogonal) curvilinear

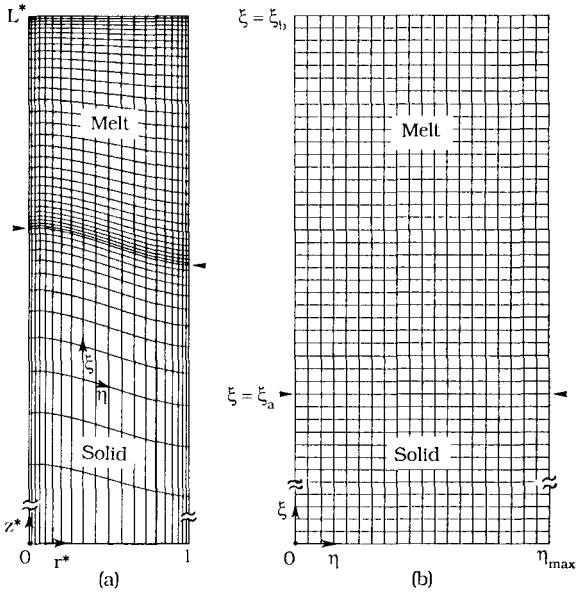

Figure 3. Part of a 21 × 51 grid mesh used for computation of heat transfer and fluid flow in the half-zone system: (a) physical domain; (b) computational domain. The melt/solid interface (indicated by arrowheads) coincides with a grid line in both cases

co-ordinates (η, ξ), which fits all the physical boundaries, including the melt/solid interface, as shown in Figure 3. In this way, all the boundary conditions can be treated accurately. The generation of the grid shown in Figure 3(a) will be discussed later.

Following the procedure of Thompson *et al.*,[33] equations (3)–(5) can be transformed into the following general form:

$$\frac{\partial}{\partial\eta}\left(a\phi\frac{\partial\psi^*}{\partial\xi}\right)-\frac{\partial}{\partial\xi}\left(a\phi\frac{\partial\psi^*}{\partial\eta}\right)+\frac{b}{J}\left(g_{22}\frac{\partial^2(c\phi)}{\partial\eta^2}+g_{11}\frac{\partial^2(c\phi)}{\partial\xi^2}\right)+d_{PQ}+d_{nor}+d_{or}=0. \tag{6}$$

Coefficients a, b, c and d in the above equation are given in Table I for $\phi=\psi^*$, ω^* and θ respectively. Other coefficients in the same equation are defined as follows:

$$d_{PQ}=bJ\left(P(\eta,\xi)\frac{\partial(c\phi)}{\partial\eta}+Q(\eta,\xi)\frac{\partial(c\phi)}{\partial\xi}\right),$$

$$d_{nor}=-\frac{2bg_{12}}{J}\frac{\partial^2(c\phi)}{\partial\eta\partial\xi}+\frac{1}{J}\left[\left(g_{22}\frac{\partial b}{\partial\eta}-g_{12}\frac{\partial b}{\partial\xi}\right)\frac{\partial(c\phi)}{\partial\eta}+\left(g_{11}\frac{\partial b}{\partial\xi}-g_{12}\frac{\partial b}{\partial\eta}\right)\frac{\partial(c\phi)}{\partial\xi}\right],$$

$$d_{or}=Jd,$$

$$g_{11}=\left(\frac{\partial r^*}{\partial\eta}\right)^2+\left(\frac{\partial z^*}{\partial\eta}\right)^2,$$

$$g_{22}=\left(\frac{\partial r^*}{\partial\xi}\right)^2+\left(\frac{\partial z^*}{\partial\xi}\right)^2,$$

$$g_{12}=\left(\frac{\partial r^*}{\partial\eta}\right)\left(\frac{\partial r^*}{\partial\xi}\right)+\left(\frac{\partial z^*}{\partial\eta}\right)\left(\frac{\partial z^*}{\partial\xi}\right),$$

$$J=\left(\frac{\partial r^*}{\partial\eta}\right)\left(\frac{\partial z^*}{\partial\xi}\right)-\left(\frac{\partial z^*}{\partial\eta}\right)\left(\frac{\partial r^*}{\partial\xi}\right),$$

$$P=-\left(\frac{\partial^2 r^*}{\partial\eta^2}\right)\Big/\left(\frac{\partial r^*}{\partial\eta}\right)^3,$$

$$Q=\left[\left(\frac{\partial z^*}{\partial\xi}\frac{\partial z^*}{\partial\eta}\frac{\partial^2 r^*}{\partial\eta^2}-\frac{\partial z^*}{\partial\xi}\frac{\partial r^*}{\partial\eta}\frac{\partial^2 z^*}{\partial\eta^2}\right)+2\left(\frac{\partial r^*}{\partial\eta}\frac{\partial z^*}{\partial\eta}\frac{\partial^2 z^*}{\partial\eta\partial\xi}\right)-g_{11}\left(\frac{\partial r^*}{\partial\eta}\frac{\partial^2 z^*}{\partial\xi^2}\Big/\frac{\partial z^*}{\partial\xi}\right)\right]\Big/\left[\left(\frac{\partial r^*}{\partial\eta}\right)^3\left(\frac{\partial z^*}{\partial\xi}\right)^2\right].$$

The above expressions for P and Q are not general but are valid only when $\partial r/\partial\xi$ is zero, which is the case in the present study.

Table I. Coefficients a, b, c and d in equation (6)

ϕ	a	b	c	d
ψ^*	0	$1/\rho r^*$	1	ω^*
ω^*	$1/r^*$	$1/r^*Re$	r^*	$-(Gr/Re^2)\partial\theta/\partial r^*$
θ	1	$r^*/PrRe$	1	0

The transformed thermal boundary conditions (with $\partial r/\partial \xi = 0$) are as follows.

1. Along the centreline of the system,

$$\frac{\partial \theta}{\partial \eta} = 0.$$

2. On the surfaces of the sample rod and the free surface of the melt,

$$-(\mathbf{n} \cdot \nabla^* \theta) = Bi(\theta - \theta_a).$$

3. At the melt/heater interface,

$$\theta = 1.$$

4. At the melt/solid interface,

$$\theta = 0, \qquad (k^* \mathbf{n} \cdot \nabla^* \theta)_S - (\mathbf{n} \cdot \nabla^* \theta)_L = 0.$$

The transformed fluid flow boundary conditions (with $\partial r/\partial \xi = 0$) are as follows.

1. Along the melt centreline,

$$\psi^* = 0, \qquad \omega^* = 0.$$

2. On the melt free surface,

$$\psi^* = 0, \qquad \omega^* = -\left(Ma^{1/3} \frac{\partial \theta}{\partial \xi} \right) \Big/ \frac{\partial z}{\partial \xi}.$$

3. At the melt/heater interface,

$$\psi^* = 0, \qquad \omega^* = -\frac{g_{11}}{r^* J^2} \frac{\partial^2 \psi^*}{\partial \xi^2}.$$

4. At the melt/solid interface,

$$\psi^* = 0, \qquad \omega^* = -\frac{g_{11}}{r^* J^2} \frac{\partial^2 \psi^*}{\partial \xi^2}.$$

METHOD OF SOLUTION

Regarding the grids for computation, one can generate the grid in Figure 3(a) by numerically solving two Laplace equations, as demonstrated by Thompson *et al.*[33] However, since the shape of the physical system in the present study is relatively simple, we have decided to use a simple but efficient approach as described below. Another reason for using the grid-spacing algorithm is that it allows second-order accuracy in the finite difference computation.

A grid system in the computational domain is first constructed as shown in Figure 3(b). η increases from zero at the centreline to η_{max} at the melt surface, while ξ increases from zero at the bottom of the sample rod to ξ_a at the melt/solid interface and then to ξ_b at the melt/heater interface. This grid spacing $\Delta\eta = \Delta\xi =$ constant in order to insure second-order accuracy in the finite difference approximations. Simple analytical equations can be used to relate r^* to η and z^* to ξ respectively, as shown in the following example:

$$r^* = 0{\cdot}5\{1 + \tanh[c(\eta/\eta_{max} - 0{\cdot}5)]/\tanh(0{\cdot}5c)\}, \tag{7}$$

solid

$$z^* = h_L^*[1-(k_c^{(NPY1-1)(1-\xi/\xi_a)}-1)/(k_c^{(NPY1-1)}-1)], \tag{8}$$

melt

$$z^* = h_L^* + 0{\cdot}5(L^*-h_L^*)\left\{1+\tanh\left[C\left(\frac{\xi-\xi_a}{\xi_b-\xi_a}-0{\cdot}5\right)\right]\Big/\tanh(0{\cdot}5C)\right\}, \tag{9}$$

where h_L^* and L^* are the dimensionless heights of the melt/solid and the melt/heater interfaces, the former being a function of η while the latter is a constant. NPY1 is the number of nodal points in the ξ-direction in the solid. The values of 3·0 for the constants C and c and 1·25 for the constant k_c have been found satisfactory for the present problem.

It should be pointed out that the r^*–η and z^*–ξ relationships in equations (7)–(9) (including the values of the constants) are so set up as to help produce finer grid spacing near the melt/solid interface and all other boundaries of the system, as shown in Figure 3(a). It should also be pointed out that the first and second derivatives of r^* (with respect to η) and z^* (with respect to ξ), which appear many times in the coefficients in equation (6), can be derived from equations (7)–(9). The derivatives so obtained are more accurate since no finite difference approximations are needed.

Before proceeding to describe the numerical method used in the present study, it should be mentioned that Brown and his co-workers have studied free boundary problems in crystal growth, especially those associated with the Bridgman and Czochralski processes (see e.g. References 29, 34 and 35). The numerical methods they have developed, which are based on the finite element method, can also be applied to solve the present problem. However, since we have always been working with the finite difference method, we have chosen to use this method in the present study.

The numerical method of Gosman *et al.*[32] was employed. In brief, equation (6) was integrated over the control volume shown in Figure 4 and then discretized to obtain the following finite

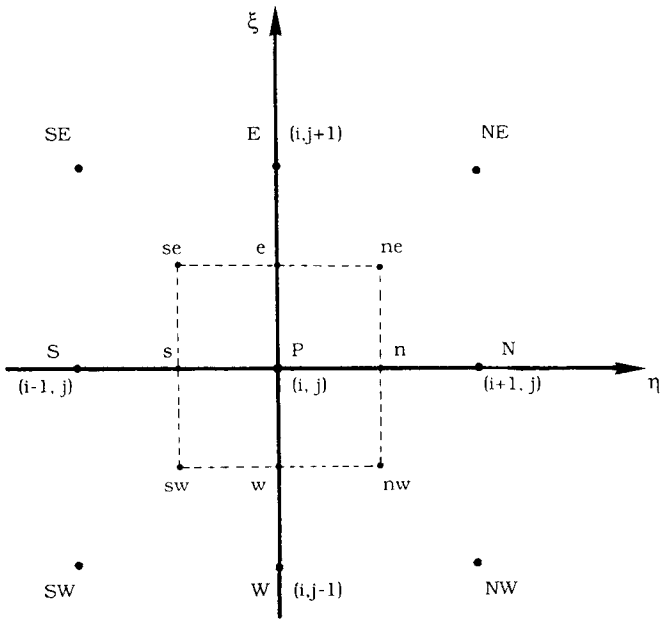

Figure 4. Illustration of a portion of the finite difference grid showing the control volume

difference equation:

$$\phi_P = C_E\phi_E + C_W\phi_W + C_N\phi_N + C_S\phi_S + D, \tag{10}$$

where

$$C_E = (A_E + B_E c_{\phi,E})/\sum_{AB},$$
$$C_W = (A_W + B_W c_{\phi,W})/\sum_{AB},$$
$$C_N = (A_N + B_N c_{\phi,N})/\sum_{AB},$$
$$C_S = (A_S + B_S c_{\phi,S})/\sum_{AB},$$
$$D = d_{\phi,P} V_P/\Sigma_{AB}$$

and

$$\Sigma_{AB} = A_E + A_W + A_N + A_S + c_{\phi,P}(B_E + B_W + B_N + B_S),$$
$$d_{\phi,P} = d_{PQ} + d_{nor} + d_{or},$$
$$V_P = (\eta_N - \eta_S)(\xi_E - \xi_W)/4.$$

In the above equations,

$$A_E = (a_P/8)[(\psi_{SE} + \psi_S - \psi_{NE} - \psi_N) + |\psi_{SE} + \psi_S - \psi_{NE} - \psi_N|],$$
$$A_W = (a_P/8)[(\psi_{NW} + \psi_N - \psi_{SW} - \psi_S) + |\psi_{NW} + \psi_N - \psi_{SW} - \psi_S|],$$
$$A_N = (a_P/8)[(\psi_{NE} + \psi_E - \psi_{NW} - \psi_W) + |\psi_{NE} + \psi_E - \psi_{NW} - \psi_W|],$$
$$A_S = (a_P/8)[(\psi_{SW} + \psi_W - \psi_{SE} - \psi_E) + |\psi_{SW} + \psi_W - \psi_{SE} - \psi_E|],$$
$$B_E = \left(\frac{bg_{11}}{2J}\right)_P \frac{\eta_N - \eta_S}{\xi_E - \xi_P},$$
$$B_W = \left(\frac{bg_{11}}{2J}\right)_P \frac{\eta_N - \eta_S}{\xi_P - \xi_W},$$
$$B_N = \left(\frac{bg_{22}}{2J}\right)_P \frac{\xi_E - \xi_W}{\eta_N - \eta_P},$$
$$B_S = \left(\frac{bg_{22}}{2J}\right)_P \frac{\xi_E - \xi_W}{\eta_P - \eta_S}.$$

The absolute values in A_E, A_W, A_S and A_N are due to the use of the upwind scheme. The above equations are very similar to those given by Gosman *et al.*[32]

The relaxation factor, called the E-factor, introduced by Raithby and Schneider[36] was employed. With this, equation (10) can be rewritten as follows:

$$\phi_P = \frac{\text{RHS} + (J/E)\phi_P^{\text{old}}}{1 + J/E}, \tag{11}$$

where RHS is the right-hand side of equation (10). The Jacobian J appears in equation (11) because of co-ordinate transformation. Various values of E can be used, but 0·5 was found to work well in our calculations.

The melt/solid interface was located and updated using the isotherm migration method, which has been described by Crank.[37] Essentially, the Stefan condition described previously was used in

each iteration of the temperature field calculation. After the temperature field was calculated, a new interface was then located by the following linear interpolation (when $\theta_{i,j} \leqslant 0$ and $\theta_{i,j+1} > 0$):

$$h_L(\eta_i) = z^*_{i,j} + (z^*_{i,j+1} - z^*_{i,j})(0 - \theta_{i,j})/(\theta_{i,j+1} - \theta_{i,j}). \tag{12}$$

Based on the new interface, a new grid mesh was generated using equations (7)–(9), and the geometric coefficients g_{11}, g_{12}, g_{22}, J, P and Q corresponding to this new mesh were calculated. All these were then used to calculate the new velocity field in the melt. This iteration scheme is illustrated in Figure 5. Besides the outer iteration loop, there were also inner iteration loops, i.e. one for temperature, one for vorticity and one for the streamfunction. The number of iterations was about five in each of these inner loops. The outer-loop iteration was continued until the following convergence criteria were satisfied:

$$\frac{\sum|\psi^*_{\text{old}} - \psi^*|}{\sum|\psi^*|} < 1 \times 10^{-4},$$

$$\frac{\sum|\omega^*_{\text{old}} - \omega^*|}{\sum|\omega^*|} < 1 \times 10^{-4},$$

$$|\theta_{\text{old}} - \theta|_{\max} < 2 \times 10^{-4},$$

$$\sum|h^*_{L,\text{old}} - h^*_L| < 5 \times 10^{-4}.$$

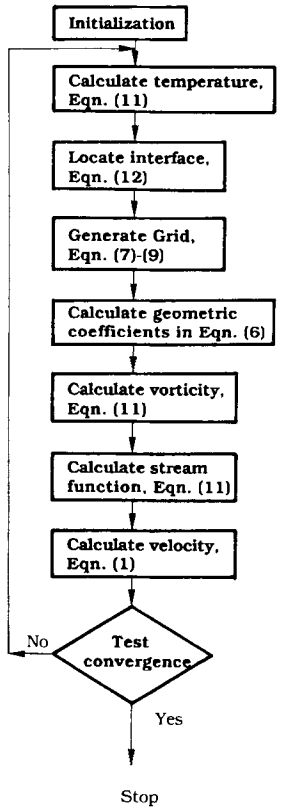

Figure 5. Flowchart showing the iteration scheme

In the first two criteria $\sum$ denotes summation over all grid points, while in the last criterion $\sum$ denotes summation over the grid points along the melt/solid interface. A Harries 800 computer was used and the CPU time ranged from 20 to 60 min depending on the extent of convection involved. This range of CPU time corresponds to approximately 30–200 times of updating the melt/solid interface.

RESULTS AND DISCUSSION

In order to check the validity of the co-ordinate transformation, grid generation and heat flow calculation, the temperature distributions in the melt and the sample rod and the shape of the melt/solid interface were calculated for the simple case where heat transfer is by conduction only and where the thermal properties of the solid and the melt are identical. The analytical solution for the dimensionless temperature in this case is given by[38]

$$\theta = (1-\theta_a)\left(\sum_{n=1}^{N} \frac{2Bi\,J_0(\lambda_n r^*)}{(Bi^2+\lambda_n^2)J_0(\lambda_n)} \frac{\lambda_n \cosh(\lambda_n z^*)+Bi\sinh(\lambda_n z^*)}{\lambda_n \cosh(\lambda_n L^*)+Bi\sinh(\lambda_n L^*)}\right)+\theta_a .$$

In the above equation, λ_n is the nth root of the equation

$$\lambda J_0'(\lambda)+Bi\,J_0(\lambda)=0,$$

where J_0 is the Bessel function of the first kind and zero order, and J_0' is its first derivative. To insure accuracy, a total of 100 roots (i.e. $N=100$) are used to calculate the dimensionless temperature θ. The agreement between the numerical solution and the analytical solution given above is excellent, an example being shown in Figure 6 for a 6 mm diameter, 40 mm long rod of $NaNO_3$. The Biot number is $4{\cdot}83\times10^{-3}$ and is based on a heat transfer coefficient of 4600 erg cm^{-2} s^{-1} °C^{-1} at an average air temperature of 600 K.[39] It should be pointed out that the heat transfer coefficient at the bottom of the solid sample rod is taken to be the same as that on its surface. This is equivalent to the case where the solid sample rod is held in position by

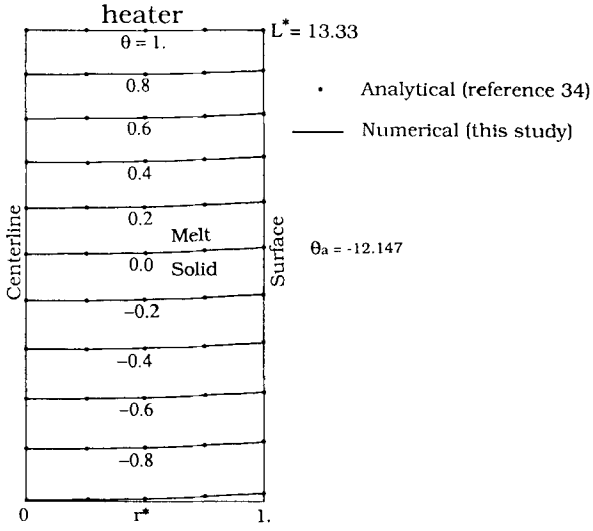

Figure 6. Comparison between analytical and numerical solutions of dimensionless temperature θ

horizontal set screws with a sharp point. A different heat transfer coefficient may be used if the bottom is in direct contact with a horizontal surface.

In order to test the effect of the grid mesh, we have used two significantly different grid meshes for computation. The first one, which is shown in part in Figure 3, is 21 × 51. The second one, which is shown in part in Figure 7, is 41 × 71. The calculated results (for $Gr=0$, $Ma=-167$ and $Pr=1{\cdot}86$) based on the first and second grid meshes are shown in Figure 8(a) and 8(b) respectively. As shown, the streamlines near the centre of the vortex are smoother in Figure 8(b) owing to there being significantly more grid points in the melt. Speaking overall, however, the results shown in the two cases are very close, the difference being less than 3%. In fact, the shape and position of the melt/solid interface and the position of the vortex are almost identical in the two cases. In order to save computation time, we have decided to adopt the 21 × 51 grid mesh for computation.

Before proceeding to discuss the calculated results, it is perhaps useful to give an indication about the level of velocities involved in the computation. Using the results shown in Figure 8(b) as an example, the fastest flow is 0·635 cm s^{-1}, which is located at the mid-height of the free surface and points vertically downwards.

The values of the variables used in the calculations are listed in Table II. These values are close to those cited for $NaNO_3$ by Schwabe *et al.*[2] Since no distinctions between the thermal properties of solid and liquid were made in the data provided by Schwabe *et al.*,[2] the same thermal properties were used for both solid and liquid. It is, however, recognized that the mismatch in thermal properties (especially the thermal conductivity) can affect the melt/crystal interface shape. A significantly lower thermal conductivity (k) of $5{\cdot}71 \times 10^4$ erg $cm^{-1}\,°C^{-1}\,s^{-1}$ and somewhat different β and $\partial\gamma/\partial T$ were also cited by the same group of investigators elsewhere (see e.g. Reference 4). It should be pointed out that instead of using $\partial\gamma/\partial T=-0{\cdot}07$ dyn $cm^{-1}\,°C^{-1}$ cited for $NaNO_3$ by Schwabe *et al.*,[2] we have chosen to use $\partial\gamma/\partial T=-0{\cdot}01$ dyn $cm^{-1}\,°C^{-1}$ in order to

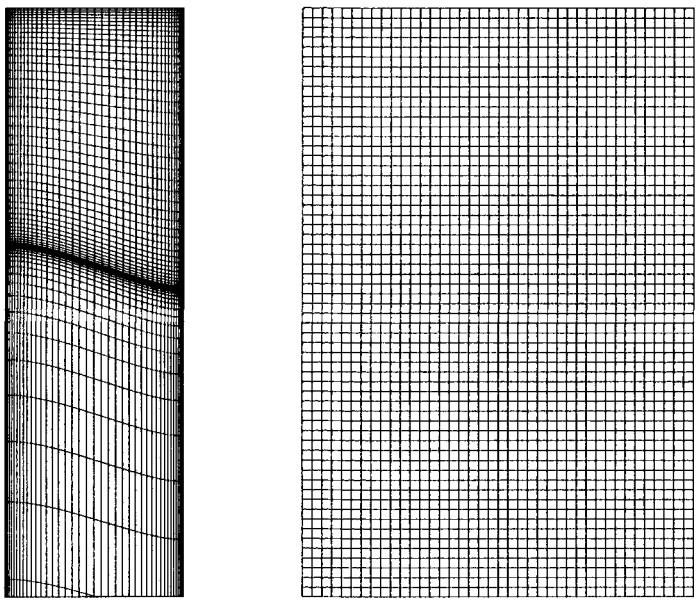

Figure 7. Part of a 41 × 71 grid mesh used for computation: (a) physical domain; (b) computational domain

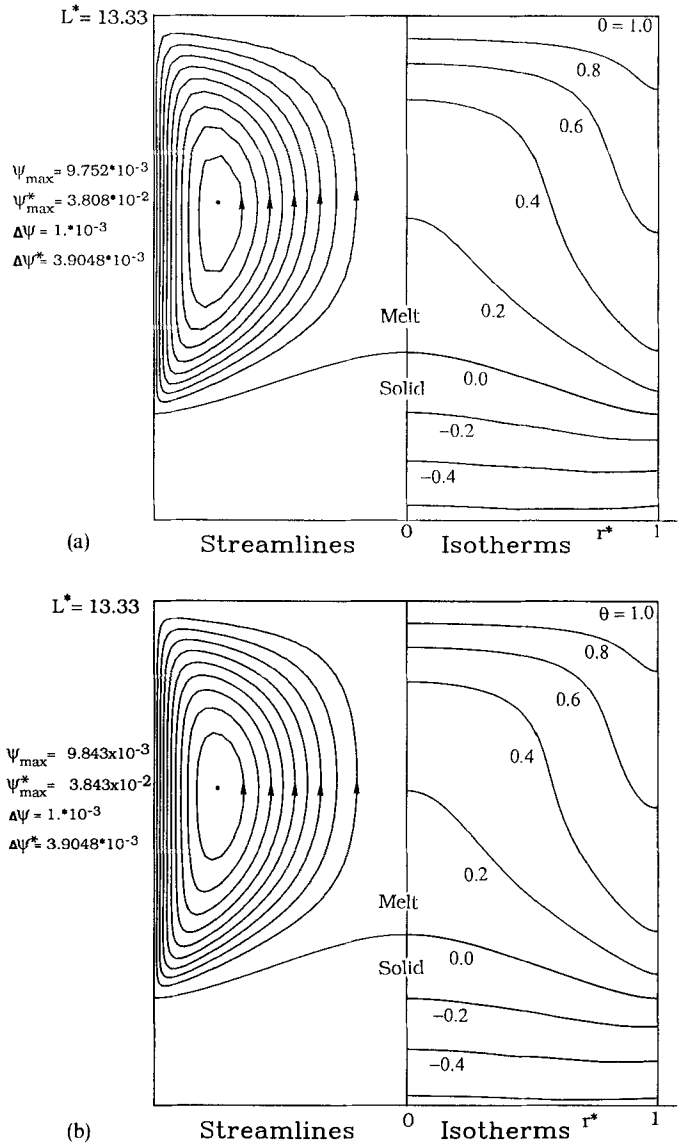

Figure 8. Effect of the grid mesh on calculated results: (a) the 21 × 51 grid mesh shown in Figure 3; (b) the 41 × 71 grid mesh shown in Figure 7

Table II. Values of variables used for computation

c_p	$1{\cdot}88 \times 10^{7}$ erg °C^{-1} g^{-1}	β	$6{\cdot}6 \times 10^{-4}$ °C^{-1}
h†	4600 erg cm^{-2} s^{-1} °C^{-1}	$\partial\gamma/\partial T$	$-0{\cdot}01$ dyn cm^{-1} °C^{-1}
ΔH	$1{\cdot}85 \times 10^{9}$ erg g^{-1}	μ	$2{\cdot}82 \times 10^{-2}$ g cm^{-1} s^{-1}
k	$2{\cdot}86 \times 10^{5}$ erg cm^{-1} °C^{-1} s^{-1}	ρ_L	1·90 g cm^{-3}
T_m	306·8 °C	ρ_S	1·90 g cm^{-3}
R	0·3 cm		

† Reference 36 and 600 K.

avoid computing steady-state flow in an $NaNO_3$ melt where we have actually observed instability due to rather strong oscillatory (unsteady-state) thermocapillary flow. The purpose of the present study is not specifically for $NaNO_3$ and this is obvious since the values in Table II are varied in order to demonstrate the effects of certain dimensionless numbers.

The effect of the Grashof number *Gr* is shown in Figure 9. From Figure 9(a) to 9(b) to 9(c), *Gr* increases from zero to 923 to 1845. The Marangoni number *Ma* and the Prandtl number *Pr* remain constant at -167 and 1·86 respectively. The melt temperature at the melt/heater interface is $T_h = 330\,^{\circ}C$. Since T_m is chosen to be the melting point of $NaNO_3$, i.e. 306·8 °C, the character-

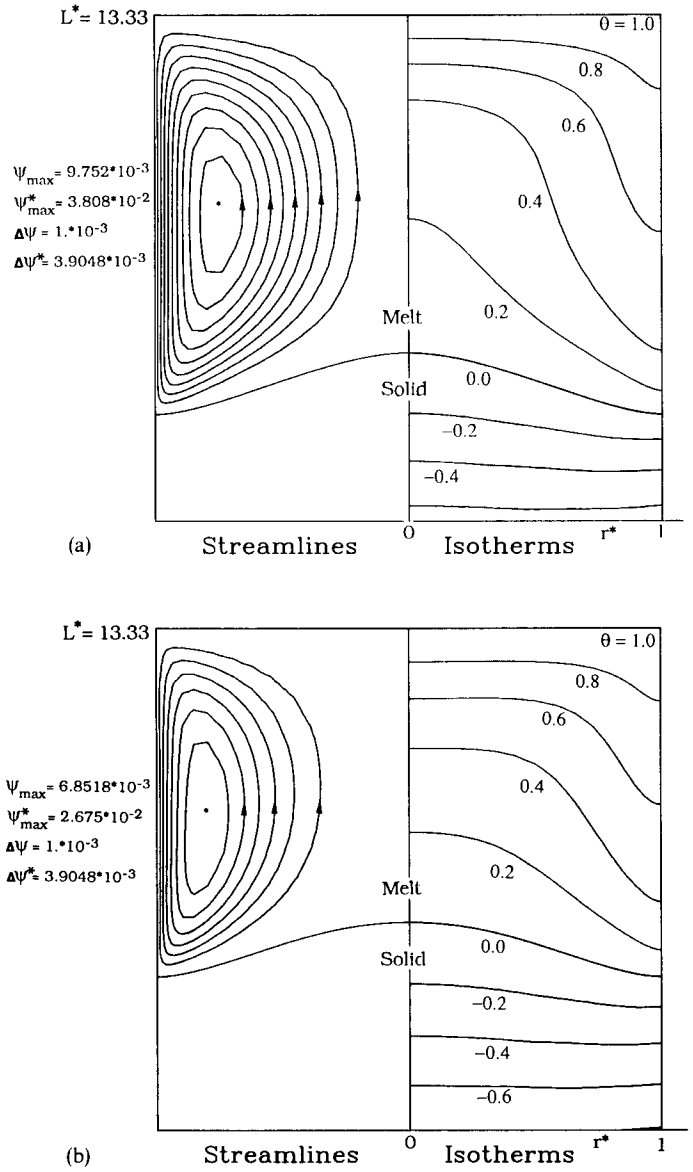

Figure 9. (a–b)

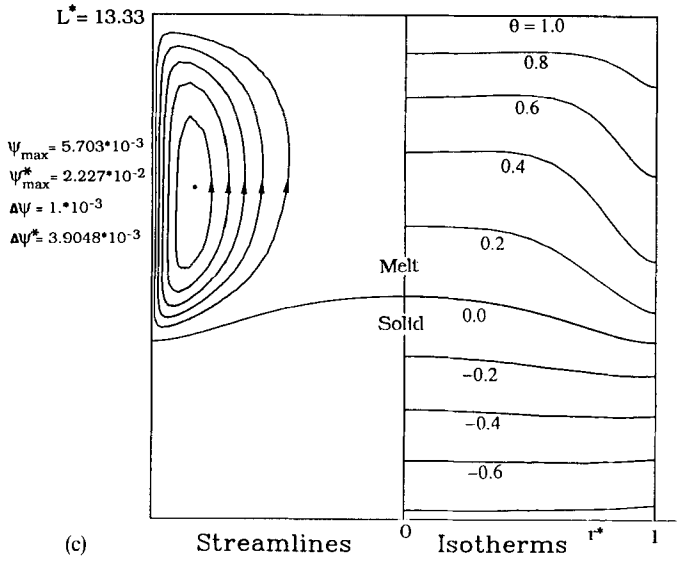

Figure 9. Effect of the Grashof number Gr: (a) $Gr=0$; (b) $Gr=923$; (c) $Gr=1845$. $Ma=-167$ and $Pr=1{\cdot}86$

istic temperature difference ΔT is 23·2 °C. The zero value of Gr represents the case where the system is under microgravity ($g=0$) or the thermal expansion coefficient of the melt is zero ($\beta=0$). As shown in Figure 9(a), thermocapillary flow prevails in the melt. The melt flows downwards along the free surface, i.e. from the hotter area to the cooler one, since Ma (and $\partial\gamma/\partial T$) is negative. The return flow is upwards along the centreline. The maximum streamfunction is $\psi^*=3{\cdot}81\times10^{-2}$ or $\psi=9{\cdot}75\times10^{-3}\,\mathrm{g\,s^{-1}}$.

The temperature field corresponding to $Gr=0$ is also shown in Figure 9(a). The melt/solid interface is represented by the line of zero dimensionless temperature θ. Owing to the action of the thermocapillary flow described above, the isotherms in the melt are pushed downwards near the free surface but upwards near the centreline. This results in three things. First, the melt/solid interface is distorted, i.e. convex toward the melt. Secondly, the axial temperature gradient along the melt/heater interface is steepened (i.e. becomes more positive), except in the small area near the free surface. Thirdly, the radial temperature gradient in the melt is increased (i.e. becomes more positive).

Referring to Figure 9(b), as the Grashof number Gr is increased to 923, natural convection comes into play. This is due to the relatively high radial temperature gradients in the melt set up by the thermocapillary flow. However, the direction of this natural convection is opposite to that of the thermocapillary flow, i.e. upwards near the melt surface (where the melt is hotter) and downwards near the centreline (where the melt is cooler). Consequently, the strength of thermocapillary flow is reduced, the maximum streamfunction being decreased to $\psi^*=2{\cdot}67\times10^{-2}$ or $\psi=6{\cdot}85\times10^{-3}\,\mathrm{g\,s^{-1}}$. The melt/solid interface is less convex than that in Figure 9(a). Furthermore, the melt column is considerably shorter than that in Figure 9(a). This is because the average axial temperature gradient along the melt/heater interface is no longer as steep as that in Figure 9(a). Consequently, the heat input from the heater to the melt is reduced.

As the Grashof number is further increased to 1845, the strength of thermocapillary flow is further reduced by natural convection, as shown in Figure 9(c). The maximum streamfunction is $\psi^*=2{\cdot}23\times10^{-2}$ or $\psi=5{\cdot}70\times10^{-3}\,\mathrm{g\,s^{-1}}$. Consequently, the distortions in the isotherms in the melt and the melt/solid interface are further reduced and the melt column is further shortened.

The effect of the Marangoni number Ma is shown in Figure 10. From Figure 10(a) to 10(b) to 10(c), Ma changes from -167 to $-83{\cdot}5$ to $-16{\cdot}7$. The Grashof number Gr and the Prandtl number Pr remain constant at 1845 and 1·86 respectively. The melt temperature at the melt/heater interface is $T_h = 330\,^{\circ}\mathrm{C}$, i.e. $\Delta T = 23{\cdot}2\,^{\circ}\mathrm{C}$. As expected, as the absolute value of Ma decreases, the strength of thermocapillary flow in the melt decreases. The maximum streamfunction drops from $\psi^* = 2{\cdot}23 \times 10^{-2}$ or $\psi = 5{\cdot}70 \times 10^{-3}\,\mathrm{g\,s^{-1}}$ in Figure 10(a) to $\psi^* = 2{\cdot}12 \times 10^{-2}$ or $\psi = 3{\cdot}42 \times 10^{-3}\,\mathrm{g\,s^{-1}}$ in Figure 10(b). It drops further to $\psi^* = 1{\cdot}60 \times 10^{-2}$ or $\psi = 8{\cdot}81 \times 10^{-4}\,\mathrm{g\,s^{-1}}$ in Figure 10(c). Furthermore, the distortions in the isotherms and the

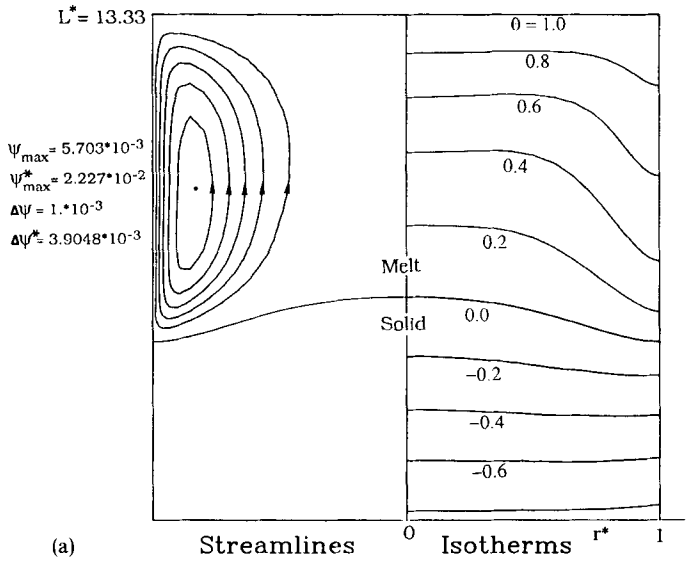

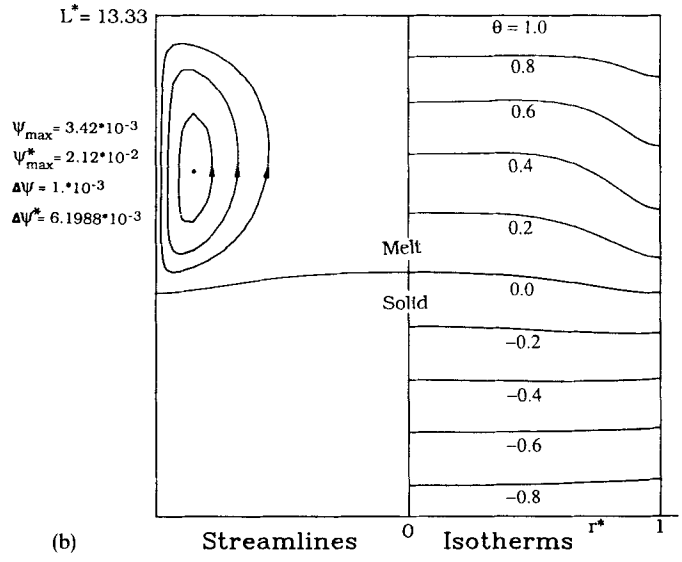

Figure 10. (a–b)

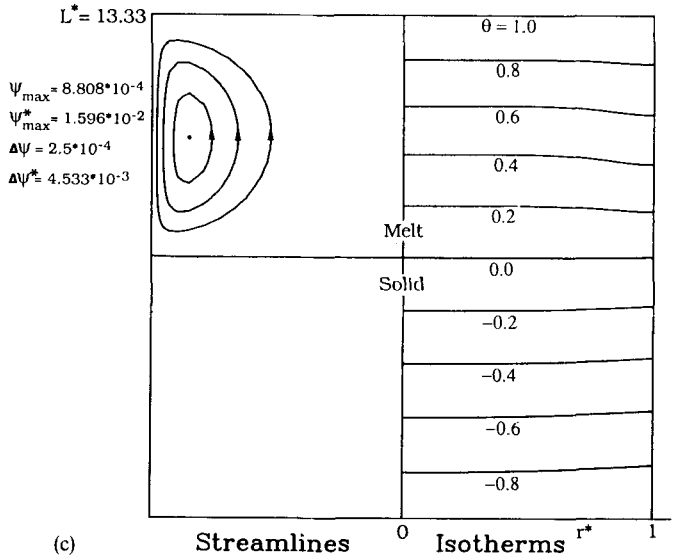

Figure 10. Effect of the Marangoni number Ma: (a) $Ma = -167$; (b) $Ma = -83{\cdot}5$; (c) $Ma = -16{\cdot}7$. $Gr = 1845$ and $Pr = 1{\cdot}86$

melt/solid interface are reduced and the melt column is shortened. The reasons for these are similar to those mentioned above in the discussion of Figure 9.

The significant reduction in the strength of thermocapillary flow mentioned above is more adequately reflected by the changes in ψ than ψ^*. For instance, Figure 10(a) to 10(c), ψ drops 84·5% while ψ^* drops only 28·3%. This is because the characteristic velocity U, which is used to define ψ^*, drops from 1·50 cm s^{-1} in Figure 10(a) to 0·94 cm s^{-1} in Figure 10(c).

It should be mentioned that the characteristic velocity has also been defined as follows:[17, 24, 26]

$$U' = \frac{|\partial\gamma/\partial T|\Delta T}{\mu}.$$

Based on this definition of the characteristic velocity, the values of the maximum dimensionless streamfunction ψ^* become $4{\cdot}05 \times 10^{-3}$, $4{\cdot}85 \times 10^{-3}$ and $6{\cdot}25 \times 10^{-3}$ for Figures 10(a), 10(b) and 10(c) respectively. This can be confusing since, going from Figure 10(a) to 10(b) to 10(c), the maximum ψ^* increases even though convection is reduced.

It should also be mentioned that the following definition of the Marangoni number has often been used (see e.g. References 18 and 24):

$$Ma' = \frac{(\partial\gamma/\partial T)\Delta T R}{\rho_L \nu^2} Pr.$$

As can be seen, this definition of the Marangoni number includes the Prandtl number Pr. Since we prefer discussing the effect of surfce tension, i.e. $(\partial\gamma/\partial T)\Delta T$, separately from that of the thermal diffusivity α, we have decided to choose a Marangoni number Ma which does not include the Prandtl number.

The effect of the Prandtl number Pr is shown in Figure 11. From Figure 11(a) to 11(b) to 11(c), Pr decreases from 1·86 to 0·372 to 0·186. The Grashof number Gr and the Marangoni number Ma remain constant at zero and -167 respectively. In Figure 11(a) the melt temperature at the melt/heater interface is again $T_h = 330\,^\circ$C, the characteristic temperature difference ΔT again

being 23·2 °C. The same values of T_h and ΔT, however, cannot be used any longer in Figures 11(b) and 11(c), where Pr is reduced five and ten times respectively. This is because the height of the melt column is rather sensitive to variations in Pr. When Pr is reduced significantly (ie. the thermal conductivity is increased significantly), the average axial temperature gradient in the melt is reduced significantly and the melt column becomes excessively long. In order to avoid unrealistically long melt columns, we have decided to reduce T_h to 315 °C ($\Delta T = 8{\cdot}2$ °C) and 310 °C ($\Delta T = 3{\cdot}2$ °C) in Figures 11(b) and 11(c) respectively. In order to keep the Marangoni number Ma at the same level of -167, $\partial\gamma/\partial T$ is changed from -0.01 dyn cm^{-1} °C^{-1} in Figure 11(a) to

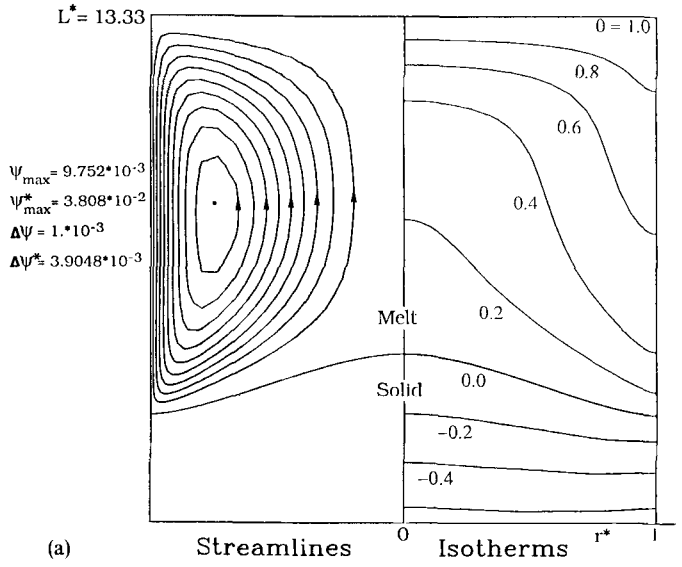

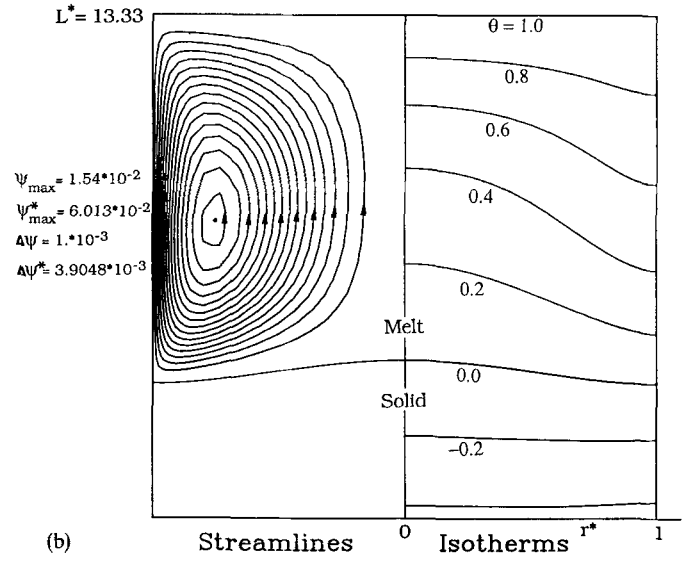

Figure 11. (a–b)

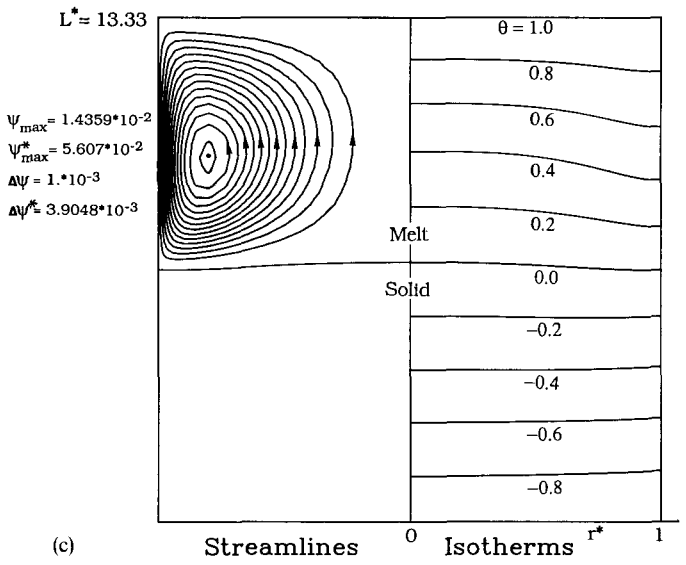

Figure 11. Effect of the Prandtl number *Pr*: (a) $Pr = 1{\cdot}86$; (b) $Pr = 0{\cdot}372$; (c) $Pr = 0{\cdot}186$. $Gr = 0$ and $Ma = -167$

$-0{\cdot}0283$ and $-0{\cdot}0725\ \mathrm{dyn\,cm^{-1}\,°C^{-1}}$ in Figures 11(b) and 11(c) respectively. The maximum streamfunctions are $\psi^* = 3{\cdot}81 \times 10^{-2}$ or $\psi = 9{\cdot}75 \times 10^{-3}\ \mathrm{g\,s^{-1}}$ in Figure 11(a), $\psi^* = 6{\cdot}01 \times 10^{-2}$ or $\psi = 1{\cdot}54 \times 10^{-2}\ \mathrm{g\,s^{-1}}$ in Figure 11(b) and $\psi^* = 5{\cdot}61 \times 10^{-2}$ or $\psi = 1{\cdot}44 \times 10^{-2}\ \mathrm{g\,s^{-1}}$ in Figure 11(c). The stronger thermocapillary flows in Figures 11(b) and 11(c) are mainly due to the more negative values of $\partial\gamma/\partial T$. Owing to the lower values of *Pr* in Figures 9(b) and 9(c), however, the isotherms in the melt and the melt/solid interface are less distorted.

Finally, it is interesting to note that for most cases shown in Figures 9–11 the melt/solid interface is convex towards the melt. However, according to the approach based on conduction only, i.e. Figure 6, it is concave towards the melt. Therefore the conduction approach appears to be a poor approximation unless the Marangoni number *Ma* and the Prandtl number *Pr* are both very low. In actual crystal growth the shape of the melt/solid interface is an important factor affecting the quality of crystals.

CONCLUSIONS

1. A computer model has been developed for steady state, axisymmetrical thermocapillary flow and natural convection in a half-zone system with an unknown melt/solid interface.
2. Natural convection can be induced by the radial temperature gradients produced by thermocapillary flow in the melt column. This natural convection, which is in the opposite direction to the thermocapillary flow, tends to reduce the strength of the latter, the distortion in the melt/solid interface and the height of the melt column.
3. With the same melt temperature at the melt/heater interface, the higher the absolute value of the Marangoni number *Ma*, the stronger is the thermocapillary flow, the more distorted the melt/solid interface and the longer the melt column.
4. The height of the melt column is rather sensitive to variations in the Prandtl number *Pr*. With the same melt temperature at the melt/heater interface, the height of the melt column tends to increase significantly with decreasing *Pr*.

5. Conduction alone cannot properly describe heat transfer in the melt, especially the shape of the melt/solid interface, unless the Marangoni number Ma and the Prandtl number Pr are both very small.

ACKNOWLEDGEMENTS

This research was supported by NASA under contract NAG8-705. We appreciate the critical comments of the reviewer.

APPENDIX: NOMENCLATURE

Bi	Biot number
C_p	specific heat
g	gravitational acceleration
Gr	Grashof number
h	heat transfer coefficient
h_L	height of melt/solid interface
ΔH	heat of fusion per unit solid mass
k	thermal conductivity
L	length of sample rod
Ma	Marangoni number
$\mathbf{n}$	unit normal vector
Pr	Prandtl number
r	cylindrical co-ordinate
R	radius of sample rod
Re	Reynolds number
T	temperature
T_a	ambient temperature
T_h	melt temperature at melt/heater interface
T_m	melting point
ΔT	characteristic temperature difference
u	r-component of velocity
U	characteristic velocity
v	z-component of velocity
$\mathbf{V}$	velocity of sample rod
z	cylindrical co-ordinate

Greek symbols

α	thermal diffusivity
β	thermal expansion coefficient
γ	surface tension
η	curvilinear co-ordinate
θ	dimensionless temperature
θ_a	dimensionless ambient temperature
μ	viscosity
ν	kinematic viscosity
ξ	curvilinear co-ordinate

ρ density
ψ streamfunction
ω vorticity

Superscripts

* dimensionless quantity

Subscripts

L liquid or melt
S solid
W wall

REFERENCES

1. C. W. Lan, Y. J. Kim and S. Kou, 'A half-zone study of Marangoni convection in floating-zone crystal growth under microgravity', *J. Cryst. Growth*, in the press.
2. D. Schwabe, A. Scharmann, F. Preisser and R. Oeder, 'Experiments on surface tension driven flow in floating zone melting', *J. Cryst. Growth*, **43**, 305–312 (1978).
3. D. Schwabe and A. Scharmann, 'Some evidence for the existence and magnitude of a critical Marangoni number for the onset of oscillatory flow in crystal growth melts', *J. Cryst. Growth*, **46**, 125–131 (1979).
4. F. Preisser, D. Schwabe and A. Scharmann, 'Steady and oscillatory thermocapillary convection in liquid columns with free cylindrical surface', *J. Fluid Mech.*, **126**, 545–567 (1983).
5. C. H. Chun and W. Wuest, 'A micro-gravity simulation of Marangoni convection', *Acta Astronaut.*, **5**, 681–686 (1978).
6. C. H. Chun and W. Wuest, 'Experiments on the transition from the steady to the oscillatory Marangoni-convection of a floating zone under reduced gravity effect', *Acta Astronaut.*, **6**, 1073–1082 (1979).
7. C. H. Chun, 'Marangoni convection in a floating zone under reduced gravity', *J. Cryst. Growth*, **48**, 600–610 (1980).
8. C. H. Chun, 'Experiments on steady and oscillatory temperature distribution in a floating zone due to Marangoni convection', *Acta Astronaut.*, **17**, 479–488 (1980).
9. C. H. Chun and W. Wuest, 'Suppression of temperature oscillations of thermal Marangoni convection in a floating zone by superimposing of rotating flows', *Acta Astronaut.*, **9**, 225–230 (1982).
10. Y. Kamotani, S. Ostrach and M. Vargas, 'Oscillatory thermocapillary convection in simulated floating-zone configuration', *J. Cryst. Growth*, **66**, 83–90 (1984).
11. Y. Kamotani and J. Kim, 'Effect of zone rotation and oscillatory thermocapillary flow in simulated floating zones', *J. Cryst. Growth*, **87**, 62–68 (1988).
12. S. Ostrach, Y. Kamotani and C. L. Lai, 'Oscillatory thermocapillary flows', *Physicochem. Hydrodyn.*, **6**, 585–599 (1985).
13. G. H. Harriott and R. A. Brown, 'Steady solute fields induced by differential rotation in a small floating zone', *J. Cryst. Growth*, **69**, 589–604 (1984).
14. J. Y. Murthy, 'A numerical simulation of flow, heat and mass transfer in a floating zone at high rotational Reynolds numbers', *J. Cryst. Growth*, **83**, 23–34 (1987).
15. J. Y. Murthy, 'The influence of secondary convection on axial segregation in a floating zone', *Trans. ASME*, **110**, 662–669 (1988).
16. N. Kobayashi, 'Computer simulation of the steady flow in a cylindrical floating zone under low gravity', *J. Cryst. Growth*, **66**, 63–72 (1984).
17. B. Fu and S. Ostrach, 'Numerical solutions of thermocapillary flows in floating zones', in *Transport Phenomena in Materials Processing*, ASME, New York, NY, 1983, pp. 1–9.
18. Y. Kamotani, S. Ostrach and M. Vargas, 'Oscillatory thermocapillary convection in a simulated floating-zone configuration', *J. Cryst. Growth*, **66**, 83–90 (1984).
19. M. K. Smith, 'Thermocapillary and centrifugal-buoyancy-driven motion in a rapidly rotating liquid cylinder', *J. Fluid Mech.*, **166**, 245–264 (1986).
20. P. A. Clark and W. R. Wilcox, 'Influence of gravity on thermocapillary convection in floating zone melting of silicon', *J. Cryst. Growth*, **50**, 461–469 (1980).
21. C. Chang and W. R. Wilcox, 'Inhomogeneities due to thermocapillary flow in floating zone melting', *J. Cryst. Growth*, **28**, 8–12 (1975).
22. C. Chang and W. R. Wilcox, 'Analysis of surface tension driven flow in floating zone melting', *J. Cryst. Growth*, **19**, 355–366 (1976).
23. N. Kobayashi and W. R. Wilcox, 'Computational studies of convection due to rotation in a cylindrical floating zone', *J. Cryst. Growth*, **59**, 616–624 (1982).

24. A. Rybicki and J. M. Floryan, 'Thermocapillary effects in liquid bridges. I. Thermocapillary convection', *Phys. Fluids*, **30**, 1956–1972 (1987).
25. R. Natarajan, 'Thermocapillary flows in a rotating float zone under microgravity', *AIChE J.*, **35**, 614–624 (1989).
26. L. G. Napolitano, C. Golia and A. Viviani, 'Effects of variable transport properties on thermal Marangoni flows', *Acta Astronaut.*, **13**, 661–667 (1986).
27. L. G. Napolitano, C. Golia and A. Viviani, 'Numerical solutions of unsteady thermal Marangoni flows', in *Proc. 5th Eur. Symp. on Materials Science under Microgravity*, Schloss Elmau, F.R.G., 1984, p. 251–258.
28. J. J. Derby, 'Theoretical modeling of Czochralski crystal growth', *MRS Bull.*, 29–35 (October 1988).
29. R. Brown, 'Theory of transport processes in single crystal growth from the melt', *AIChE J.*, **34**, 881–910 (1988).
30. S. Ostrach, 'Convection due to surface-tension gradients', in M. J. Rycroft (ed.), *Proc. COSPAR Space Research, Vol. 19*, Pergamon, Oxford, 1979, p. 563.
31. Z. Kozhoukharova and S. Slavchev, 'Computer simulation of the thermocapillary convection in a non-cylindrical floating zone', *J. Cryst. Growth*, **74**, 236–246 (1986).
32. A. D. Gosman, W. M. Pan, A. K. Runchal, D. B. Spalding and M. Wolfshtein, *Heat and Mass Transfer in Recirculating Flows*, Academic Press, London, 1969, pp. 18–115.
33. J. F. Thompson, F. C. Thames and C. W. Mastin, 'Boundary-fitted curvilinear coordinate systems for solution of partial differential equations on fields containing any number of arbitrary 2-dimensional bodies', *NASA Report NASA-CR-2729*, July 1977.
34. C. J. Chang and R. A. Brown, 'Natural convection in steady solidification: finite element analysis of a two-phase Rayleigh–Benard problem', *J. Comput. Phys.*, **53**, 1–27 (1984).
35. P. A. Sackinger and R. A. Brown, 'A finite element method for analysis of fluid flow, heat transfer and free interfaces in Czochralski crystal growth', *Int. j. numer. methods fluids*, **9**, 453–492 (1989).
36. G. D. Raithby and G. E. Schneider, 'Numerical solutions of problems in incompressible fluid flow: treatment of the velocity–pressure coupling', *Numer. Heat Transfer*, **2**, 417–440 (1979).
37. J. Crank, *Free and Moving Boundary Problems*, Oxford University Press, London, 1984, pp. 199–216.
38. H. S. Carslaw and J. C. Jaeger, *Conduction of Heat in Solids*, 2nd edn, Oxford University Press, London, 1959, p. 219.
39. L. C. Burmeister, *Convective Heat Transfer*, Wiley, New York, 1983, p. 583.